

Edge-controlled non-Hermitian skin effect in the modified Haldane model

Nobuhiro Ito

Department of Electronic and Physical Systems, Waseda University, Tokyo 169-8555, Japan *

Shun Uchino

Department of Electronic and Physical Systems, Waseda University, Tokyo 169-8555, Japan * and
Department of Materials Science, Waseda University, Tokyo 169-8555, Japan †

(Dated: March 3, 2026)

The hybrid skin–topological effect (HSTE) arises from the interplay between the non-Hermitian skin modes and topologically protected edge states. Here, we investigate the HSTE associated with antichiral edge states in a modified Haldane nanoribbon with gain and loss applied exclusively at the zigzag edges. We show that in antichiral systems, the HSTE originates from an imbalance of effective gain and loss between edge states and counter-propagating bulk modes, revealing a mechanism distinct from that in conventional chiral systems. Remarkably, in sufficiently narrow ribbons, gain or loss applied to only one edge induces a skin effect in the states localized at the opposite edge, demonstrating a non-Hermitian nonlocal antichiral skin effect. We further show that edge-localized dissipation can induce bulk skin modes only when \mathcal{PT} symmetry is broken, while the bulk non-Hermitian skin effect is strictly forbidden in the \mathcal{PT} -symmetric regime. By tuning the gain and loss applied solely at the edges, both the emergence and localization direction of bulk skin modes can be controlled. Our results establish a symmetry-based mechanism for controlling non-Hermitian skin effects via edge dissipation in antichiral systems.

I. INTRODUCTION

In recent years, non-Hermitian systems have attracted considerable attention owing to their unconventional spectral and topological properties [1–3]. A hallmark of non-Hermitian physics is the non-Hermitian skin effect (NHSE), in which bulk eigenstates that are extended under periodic boundary conditions (PBC) collapse to boundaries under open boundary conditions (OBC) [4, 5]. The NHSE is guaranteed by nontrivial point-gap topology characterized by spectral winding in the complex-energy plane, reflecting a fundamental breakdown of conventional bulk–boundary correspondence.

When non-Hermiticity coexists with topological band structures possessing line-gap topology, the interplay between these two distinct topological structures can give rise to the hybrid skin-topological effect (HSTE) [6, 7]. In the HSTE, topologically protected edge states acquire additional directional localization induced by non-Hermitian skin modes. So far, HSTEs have been extensively studied in systems hosting chiral or helical edge states, including models with asymmetric hopping [8–10], and bulk gain and loss [11–17], and edge-localized dissipation [18–20]. The experimental realizations have been reported in photonic crystals [21, 22], electrical circuits [23, 24], phononic crystals [25, 26], and active matter systems [27].

Recently, antichiral edge states were discovered in the *modified Haldane model* [28], where the phases imprinting in next-nearest-neighbor (NNN) hoppings are

(a) modified Haldane model (b) antichiral edge state



FIG. 1. (a) Direction of phase accumulation in the NNN hopping of the modified Haldane model. (b) Schematic illustration of antichiral edge states, which propagate in the same direction along opposite edges while counter-propagating modes reside in the bulk.

reversed on one sublattice of the celebrated Haldane model [29] [Fig. 1(a)]. Unlike conventional chiral edge states, antichiral edge states propagate in the same direction along opposite edges, while counter-propagating modes reside in the bulk to compensate the net current [30–40] [Fig. 1(b)]. The modified Haldane model has been realized in photonic crystals [41] and electrical circuits [42].

HSTE in antichiral systems remains largely unexplored. Although the HSTE associated with antichiral edge states has been predicted in an exciton-polariton system [16], its detailed mechanism remains poorly understood. Because of the existence of the bulk modes propagating in the opposite direction, the mechanism responsible for the HSTE in chiral systems cannot be directly applied, suggesting that the hybridization mechanism underlying the HSTE may be fundamentally different.

In this paper, we investigate a narrow modified Haldane nanoribbon with gain and loss introduced exclusively at the zigzag edges. We demonstrate that in antichiral systems, the HSTE originates from an imbalance

* itonobuhiro@fuji.waseda.jp

† shun.uchino@waseda.jp

of the effective gain and loss between the edge states and the counter-propagating bulk states. Remarkably, in sufficiently narrow ribbons, introducing gain (loss) exclusively on the lower edge can induce a skin effect in the upper-edge states. Since the effect arises at a spatially separated boundary, we refer to it as the *nonlocal non-Hermitian antichiral skin effect*.

Due to the narrowness of the system, edge-localized gain and loss induces the NHSE not only in the edge states but also in a large number of bulk states. We further show that bulk non-Hermitian skin modes are strictly forbidden in the \mathcal{PT} -symmetric regime and emerge only when \mathcal{PT} symmetry is broken. Notice that this relation between \mathcal{PT} symmetry and the NHSE is associated with a recent study [43]. We also point out that by tuning the edge gain and loss, both the emergence and localization direction of bulk skin modes can be systematically controlled.

This paper is organized as follows. In Sec. II, we introduce the modified Haldane nanoribbon with edge-localized gain and loss and define the model studied in this work. In Sec. III, we present the numerical results and analyze the non-Hermitian skin effect in both antichiral edge states and bulk states, clarifying the role of \mathcal{PT} symmetry. In Sec. IV, we summarize our findings and discuss their implications. The detailed analysis of the \mathcal{PT} -broken regime and the bulk NHSE in additional bands are presented in Appendixes A and B.

II. MODEL

A. Effective Hamiltonian

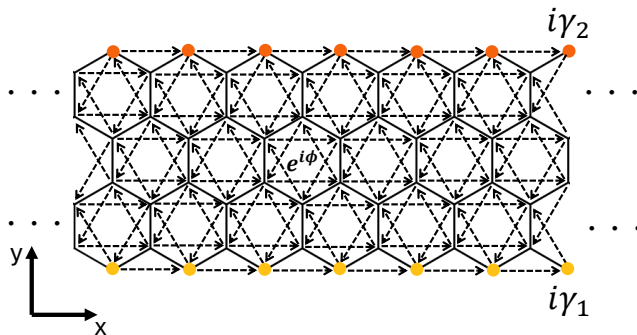


FIG. 2. Schematic of the modified Haldane nanoribbon with edge-localized gain and loss. Imaginary on-site potentials $i\gamma_1$ and $i\gamma_2$ are applied to the lower and upper zigzag edges, respectively. The dashed arrows indicate the direction of phase ϕ in the NNN hopping.

We consider a modified Haldane nanoribbon with imaginary on-site potentials introduced at the two edges, as illustrated in Fig. 2. Here we adopt the so-called zigzag edges, which host the antichiral edge states. Note that, because antichiral edge states are absent on the armchair

edges (left and right edge in Fig. 2), the two antichiral edge states remain spatially separated even under OBC. The lower (upper) edge is $i\gamma_1$ ($i\gamma_2$), representing loss or gain depending on the sign of $\gamma_{1,2}$. The effective Hamiltonian is given by

$$H(\gamma_1, \gamma_2) = -t_1 \sum_{\langle i,j \rangle} c_i^\dagger c_j - t_2 \sum_{\langle\langle i,j \rangle\rangle} e^{i\nu_{ij}\phi} c_i^\dagger c_j + i\gamma_1 \sum_{i \in \text{L-edge}} c_i^\dagger c_i + i\gamma_2 \sum_{i \in \text{U-edge}} c_i^\dagger c_i. \quad (1)$$

Here, c_i^\dagger and c_i denote the creation and annihilation operators at site i , respectively. The parameters t_1 and t_2 denote the nearest-neighbor (NN) and NNN hopping amplitudes. The sums $\langle i,j \rangle$ and $\langle\langle i,j \rangle\rangle$ run over NN and NNN pairs, respectively. The factor $\nu_{ij} = \pm 1$ specifies the direction of the phase ϕ acquired in the NNN hopping as indicated by the dashed arrows in Fig. 2. Moreover, the sets L-edge (U-edge) denote the lattice sites located on the lower (upper) zigzag edge.

Let N_x and N_y be the numbers of lattice sites along the x and y directions, respectively. Because bulk states extend throughout the system, their wave-function weight on the gain/loss sites becomes negligible in the limit $N_y \rightarrow \infty$. As a result, bulk states experience vanishing effective non-Hermiticity and do not exhibit NHSE. In contrast, the antichiral edge states remain localized at the edges, and therefore, retain sensitivity to edge gain and loss even for large N_y .

To elucidate how edge-localized gain and loss influence not only the edge states but also the bulk spectrum, we focus on a narrow ribbon with small N_y and a large N_x . In this quasi-one-dimensional geometry, the edge dissipation significantly affects all eigenstates, allowing both bulk and edge states to exhibit the NHSE. In addition, we impose OBC along y direction throughout this work. Along the x direction, we compare PBC and OBC in order to identify the emergence of the NHSE.

B. \mathcal{PT} symmetry

Under PBC along the x direction, the Hamiltonian (1) satisfies

$$(PT)H(\gamma_1, \gamma_2)(PT)^{-1} = H(-\gamma_2, -\gamma_1), \quad (2)$$

where P and T denote the inversion and time-reversal operators, respectively.

This relation follows from the intrinsic \mathcal{PT} symmetry of the modified Haldane model (Fig. 3). The NNN hopping term in Eq. (1) remains invariant under the combined \mathcal{PT} operation, since the acquired phase direction is unchanged. In contrast, the imaginary on-site potentials change sign under time reversal and are exchanged

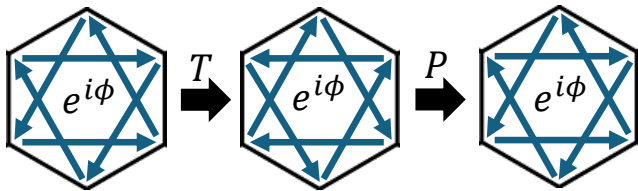


FIG. 3. Illustration of the \mathcal{PT} symmetry of the modified Haldane model. The direction of phase accumulation in the NNN hopping term is unchanged under the combined \mathcal{PT} operation, ensuring the intrinsic \mathcal{PT} symmetry of the Hermitian part of the Hamiltonian. Here, P and T denote the inversion and time-reversal operators, respectively.

between the two edges under inversion. As a result,

$$\begin{aligned}
 & (PT) \left(i\gamma_1 \sum_{i \in \text{L-edge}} c_i^\dagger c_i + i\gamma_2 \sum_{i \in \text{U-edge}} c_i^\dagger c_i \right) (PT)^{-1} \\
 &= P \left(-i\gamma_1 \sum_{i \in \text{L-edge}} c_i^\dagger c_i - i\gamma_2 \sum_{i \in \text{U-edge}} c_i^\dagger c_i \right) P^{-1} \\
 &= -i\gamma_2 \sum_{i \in \text{L-edge}} c_i^\dagger c_i - i\gamma_1 \sum_{i \in \text{U-edge}} c_i^\dagger c_i.
 \end{aligned} \tag{3}$$

Eq. (2) therefore implies that the Hamiltonian possesses \mathcal{PT} symmetry when $\gamma_1 = -\gamma_2$; otherwise, the symmetry is explicitly broken.

Let E_{γ_1, γ_2} and $\psi_{\gamma_1, \gamma_2}(x, y)$ be an eigenenergy and eigenstate of $H(\gamma_1, \gamma_2)$. Then, we have

$$H(\gamma_1, \gamma_2) \psi_{\gamma_1, \gamma_2}(x, y) = E_{\gamma_1, \gamma_2} \psi_{\gamma_1, \gamma_2}(x, y), \tag{4}$$

where (x, y) denotes the position of each lattice site. Applying the \mathcal{PT} operator yields

$$\begin{aligned}
 & H(-\gamma_2, -\gamma_1) (PT \psi_{\gamma_1, \gamma_2}(x, y)) \\
 &= E_{\gamma_1, \gamma_2}^* (PT \psi_{\gamma_1, \gamma_2}(x, y)),
 \end{aligned} \tag{5}$$

which shows that the spectra of $H(\gamma_1, \gamma_2)$ and $H(-\gamma_2, -\gamma_1)$ are complex conjugates of each other.

III. RESULT

Throughout this section, we fix $t_1 = 1$, $t_2 = 0.05$, $\phi = \pi/2$, and $N_y = 8$. We investigate three representative parameter sets:

- (i) $\gamma_1 = -0.6, \gamma_2 = +0.6$,
- (ii) $\gamma_1 = -0.6, \gamma_2 = 0$,
- (iii) $\gamma_1 = 0, \gamma_2 = +0.6$.

Case (i) satisfies the \mathcal{PT} -symmetry condition. In this regime, only the antichiral edge states exhibit the NHSE, while the bulk states remain extended. In contrast, cases (ii) and (iii) explicitly break \mathcal{PT} symmetry, allowing both edge and bulk states to develop the NHSE. The latter two cases are related to each other by the \mathcal{PT} transformation.

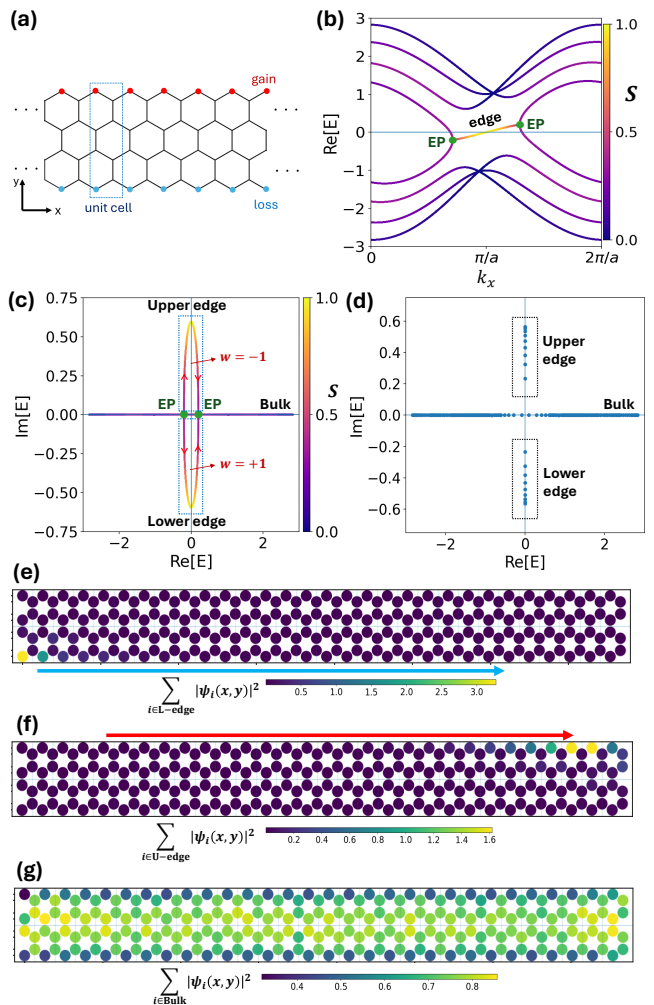


FIG. 4. Results for the \mathcal{PT} -symmetric case $H(\gamma_1 = -0.6, \gamma_2 = +0.6)$. (a) Schematic of the system. (b) Band structure of $\text{Re}[E]$ under PBC along the x direction. (c) Complex-energy spectrum under PBC. The red arrows indicate the direction of each loop as k_x increases, and w denotes the point-gap winding number. In (b) and (c), brighter colors indicate stronger localization at the upper and lower edges. The system size is $N_x = 16000$. (d) Energy spectrum under OBC along x . (e) Spatial distribution of the summed lower-edge states enclosed by the dashed rectangle in (d). (f) Spatial distribution of the summed upper-edge states enclosed by the dashed rectangle in (d). (g) Spatial distribution of the summed bulk states on the real axis in (d). In (e)-(g), brighter colors indicate higher state density. The system size is $N_x = 30$.

A. Lower-edge loss and upper-edge gain

We first consider the \mathcal{PT} -symmetric case $H(\gamma_1 = -0.6, \gamma_2 = +0.6)$, shown in Fig. 4(a). According to Eq. (2), this system satisfies the \mathcal{PT} -symmetry condition $\gamma_1 = -\gamma_2$.

1. Spectrum under PBC

Under PBC along the x direction, the Bloch wave number k_x is well defined. The real part of the band structure and the complex-energy spectrum are shown in Figs. 4(b) and 4(c), respectively. To characterize edge localization, we define

$$S = \frac{|\psi(x, y_{\min})|^2 + |\psi(x, y_{\max})|^2}{\sum_y |\psi(x, y)|^2}, \quad (6)$$

where y_{\min} and y_{\max} denote the lower and upper edges, respectively.

As seen in Fig. 4(c), all bulk eigenenergies lie on the real axis, whereas the antichiral edge states form complex-conjugate pairs. This indicates that all bulk states belong to the \mathcal{PT} -symmetric phase,

$$\mathcal{PT} \psi_{\text{bulk}}(x, y) = \psi_{\text{bulk}}^*(-x, -y) = \psi_{\text{bulk}}(x, y), \quad (7)$$

whereas the edge states are in the \mathcal{PT} -broken phase,

$$\mathcal{PT} \psi_{\text{L-edge}}(x, y) = \psi_{\text{L-edge}}^*(-x, -y) = \psi_{\text{U-edge}}(x, y). \quad (8)$$

The exceptional points (EP) separating these regions are marked in Fig. 4(b) and (c).

In Fig. 4(b), the antichiral edge states localized at the two edges appear between the two EPs, and the energies of the two edge-localized states share the same real part. Since the group velocity along the x direction is given by

$$v_x = \frac{1}{\hbar} \frac{\partial \text{Re}[E]}{\partial k_x}, \quad (9)$$

the antichiral edge states on both edges propagate in the same direction, consistent with Fig. 1(b). As the lower-edge states experience only loss sites, whereas the upper-edge states experience only gain sites, the signs of the imaginary on-site potentials are opposite, as shown in Fig. 4(c).

The upper-edge states together with some bulk states form one loop in the complex plane, while the lower-edge states together with some bulk states form another loop. The red arrows in Fig. 4(c) indicate the direction of each loop as k_x increases. The winding number

$$w(E_b) = \frac{1}{2\pi i} \int_0^{2\pi} dk_x \frac{\partial}{\partial k_x} \log \det[H(k_x) - E_b] \quad (10)$$

is +1 for the lower-edge loop and -1 for the upper-edge loop. In Eq. (10), E_b denotes the base energy, which is chosen to lie inside the loop whose winding number is evaluated. The nonzero winding numbers indicate the presence of the NHSE in the antichiral edge states. The lower-edge and upper-edge states are localized in opposite directions, since they have winding numbers with opposite signs. In contrast, most bulk states, except for those forming loops together with the edge states, do not have a point gap and therefore have zero winding number. As a result, most bulk states do not exhibit the NHSE under OBC. These extended bulk states are protected by the \mathcal{PT} symmetry because all of their eigenenergies lie on the real axis and therefore cannot open a point gap.

2. Spectrum under OBC

We now impose OBC along the x direction. In this case, the two loops observed under PBC collapse into line segments, as shown in Figs. 4(d) [44].

Under OBC, the lower-edge states localize at the left boundary, whereas the upper-edge state localize at the right boundary [Fig. 4(e) and Fig. 4(f)]. This behavior follows directly from the sign of the imaginary on-site potentials: lower-edge states experience loss and are attenuated toward the right, while upper-edge states experience gain and are amplified. The localization direction is consistent with the sign of the winding number of each loop calculated in Eq. (10). This is an HSTE induced by antichiral edge states, and it is similar to the HSTE induced by chiral edge states[11, 12, 18]. However, the HSTE induced by antichiral edge states arises from the coupling between the edge states and bulk states propagating in the opposite direction, which is clearly different from the case of chiral edge states. The details of this mechanism are described in the next subsection.

In contrast, the bulk states remain extended under OBC [Fig. 4(g)]. Consistent with the winding numbers under PBC, we find that the bulk states do not exhibit the skin effect. This phenomenon can also be understood from Eq. (7). In the \mathcal{PT} -symmetric regime, the condition

$$|\psi_{\text{bulk}}(x, y)|^2 = |\psi_{\text{bulk}}(-x, -y)|^2, \quad (11)$$

holds, preventing spatially asymmetric accumulation. Thus, \mathcal{PT} symmetry protects the bulk states from exhibiting the NHSE.

To be precise, under OBC, the shapes of the left and right edges are slightly different, as shown in Fig. 4(a). Thus, \mathcal{PT} symmetry is broken by the finite-size effect. When N_x is sufficiently large, however, the effects of the left and right edges are negligible and have little influence on the presence or absence of the skin effect.

3. Critical strength of gain/loss

By increasing γ_1 ($= -\gamma_2$), we find a critical value $|\gamma_1| = |\gamma_2| > \gamma_0 \approx 0.89$ above which bulk states enter the \mathcal{PT} -broken phase. In the main text, we restrict ourselves to the regime $|\gamma_{1,2}| < \gamma_0$, where all bulk state remain \mathcal{PT} symmetric. The \mathcal{PT} -broken regime is discussed in Appendix A.

B. Lower-edge loss

We next consider the case $H(\gamma_1 = -0.6, \gamma_2 = 0)$, shown in Fig. 5(a), where \mathcal{PT} symmetry is explicitly broken.

Under PBC, the band structure of $\text{Re}[E]$ and the energy spectrum are shown in Figs. 5(b) and 5(c), respectively. For $N_y = 8$, which is fixed throughout this study,

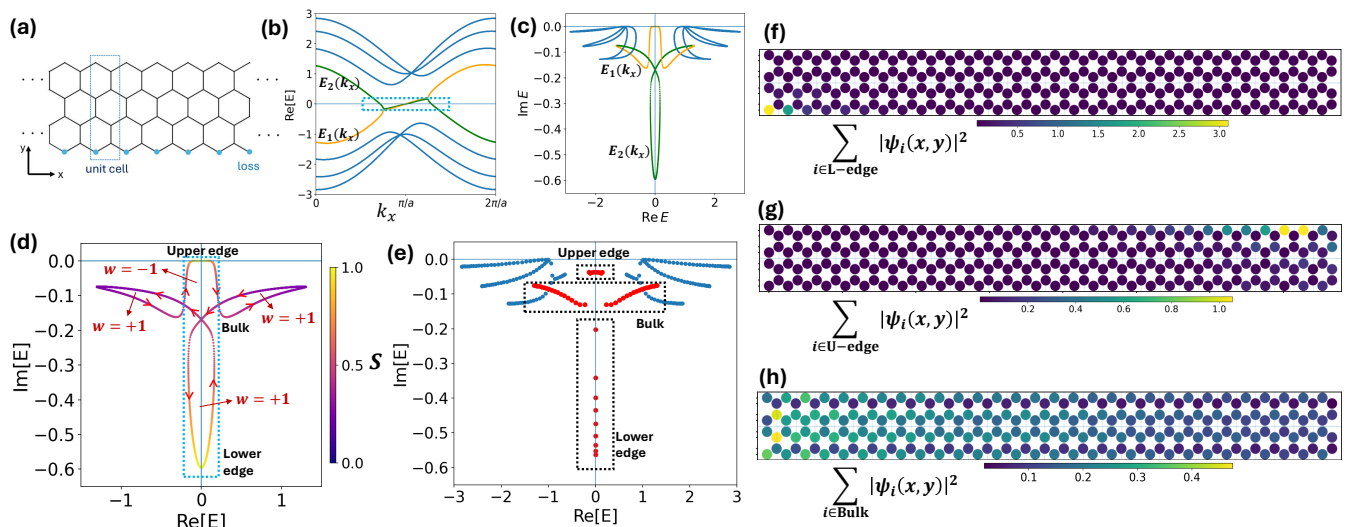


FIG. 5. Results for $H(\gamma_1 = -0.6, \gamma_2 = 0)$. (a) Schematic of the system. (b) Band structure of $\text{Re}[E]$ under PBC along the x direction. In the main text, we focus on the bands E_1 and E_2 . (c) Complex-energy spectrum under PBC. (d) Complex-energy spectrum of E_1 and E_2 under PBC. The red arrows indicate the direction of each loop as k_x increases, and w denotes the point-gap winding number. Brighter colors indicate stronger localization at the upper and lower edges. The eigenenergies enclosed by the blue dashed rectangle correspond to those enclosed in (b). The system size is $N_x = 1600$. (e) Energy spectrum under OBC along x . Red dots indicate eigenenergies originating from E_1 and E_2 in (c). (f) Spatial distribution of the summed lower-edge states enclosed by the dashed rectangle in (e). (g) Spatial distribution of the summed upper-edge states enclosed by the dashed rectangle in (e). (h) Spatial distribution of the summed bulk states (red dots) enclosed by the dashed rectangle in (e). In (f)–(h), brighter colors indicate higher state density. The system size is $N_x = 30$.

each band evolves independently under OBC without mixing with other bands[44]. We point out that for larger N_y , bulk states from different bands may hybridize under OBC, complicating the spectral evolution.

In the main text, we focus on the band containing all antichiral edge states, which appears as two branches, $E_1(k_x)$ and $E_2(k_x)$, shown in yellow and green in Fig. 5(b), respectively. These two branches form four loops in the complex-energy plane, as shown in Fig. 5(c), indicating that all eigenstates in this band exhibit the NHSE under OBC. Other bands also form loops and therefore exhibit the NHSE; their behavior is discussed in Appendix B.

We extract $E_1(k_x)$ and $E_2(k_x)$ and show their spectrum separately in Fig. 5(d). The color scale represents the quantity S defined in Eq. (6), which characterizes the degree of edge localization. The red arrows indicate the direction of evolution as k_x increases. The spectrum can be divided into two parts.

The first part, enclosed by the blue dashed rectangle in Fig. 5(d), corresponds to the same region in Fig. 5(b). From Eq. (9), this region includes all antichiral edge states propagating in the $+x$ direction, together with bulk states propagating in the $-x$ direction. For instance, at $\text{Re}[E] = 0$, two antichiral edge states propagate to the right while two bulk states propagate to the left. In Fig. 5(d), this region forms two loops: one loop contains all lower-edge states and some bulk states with the winding number $w = +1$, while the other contains

all upper-edge states and the remaining bulk states with $w = -1$.

The second part of the spectrum, located outside the blue dashed rectangle, consists purely of bulk states with both propagation directions. These states also form two loops, both with winding numbers $w = +1$, indicating that they localize in the same direction under OBC. The bulk NHSE is not forbidden here, since the system lacks \mathcal{PT} symmetry.

The energy spectrum under OBC is shown in Fig. 5(e), where the red points denote states originating from E_1 and E_2 . All four loops collapse into line segments. We group the eigenvalues into three regions (dashed rectangles in Fig. 5(e)) and plot the corresponding spatial distributions in Fig. 5(f)–5(h). The lower-edge states localize on the left side [Fig. 5(f)], while the upper-edge states localize on the right side [Fig. 5(g)]. The bulk states localize on the left side [Fig. 5(h)].

It is important to note that no gain or loss is applied to the upper edge. Nevertheless, the NHSE also emerges at the upper-edge states. Since this NHSE is induced by loss located far from the states, we call it *nonlocal non-Hermitian antichiral skin effect*.

To elucidate the mechanism of localizations, we introduce the effective gain/loss [18]

$$\gamma_{\text{eff}} = \sum_{x,y} \gamma(x,y) |\psi(x,y)|^2, \quad (12)$$

which measure the net imaginary potential experienced

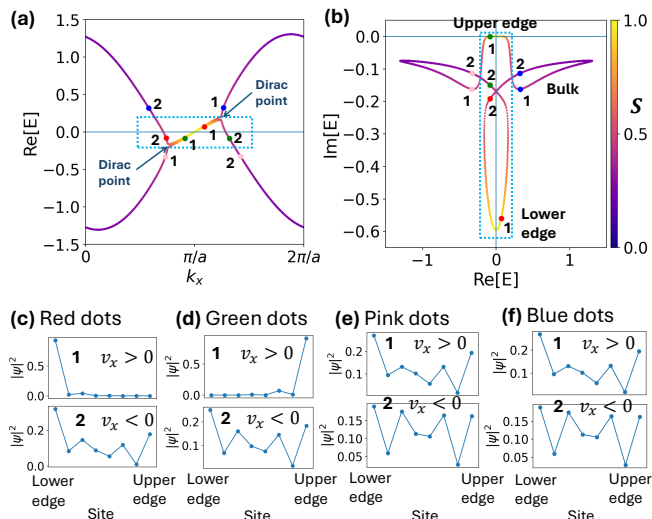


FIG. 6. Spatial profiles of representative eigenstates under PBC for $H(\gamma_1 = -0.6, \gamma_2 = 0)$. (a) Band structures of $\text{Re}[E_1]$ and $\text{Re}[E_2]$, corresponding to two branches highlighted in Fig. 5(b). (b) Complex-energy spectrum of E_1 and E_2 . The eigenenergies enclosed by the blue dashed rectangle correspond to those enclosed in (a). Brighter colors indicate stronger localization at the upper and lower edges. (c) Spatial profiles of the two red dots in (a) and (b). (d) Spatial profiles of the two green dots in (a) and (b). (e) Spatial profiles of the two pink dots in (a) and (b). (f) Spatial profiles of the two blue dots in (a) and (b). In (c)-(f), the displayed region corresponds to the sites within the unit cell shown in Fig. 5(a). v_x denotes the group velocity along the x direction of the state shown.

by a given eigenstate $\psi(x, y)$. In Eq. (12), $\gamma(x, y)$ denotes the imaginary part of the on-site potential at site (x, y) . In the present case, $\gamma(x, y) \neq 0$ only at the lower edge. For an antichiral edge state localized at the lower (upper) edge $\psi_{\text{L-edge}}(x, y)$ ($\psi_{\text{U-edge}}(x, y)$), the effective gain/loss is denoted by $\gamma_{\text{eff}}^{\text{L-edge}}$ ($\gamma_{\text{eff}}^{\text{U-edge}}$). For a bulk state $\psi_{\text{bulk}}(x, y)$, the effective gain/loss is denoted by $\gamma_{\text{eff}}^{\text{Bulk}}$.

We first discuss the origin of the NHSE in the lower-edge states. The red dots in Fig. 6(a) and 6(b) belong to the lower loop in Fig. 6(b). The corresponding eigenstate within a unit cell defined in Fig. 5(a) for dot 1 (lower-edge state) and dot 2 (bulk state) are shown in Fig. 6(c). Since the lower edge consists only of loss sites, $\gamma_{\text{eff}}^{\text{L-edge}} < 0$. From the bottom panel of Fig. 6(c), although the bulk state also has weight on the lower edge, its weight is smaller than that of the lower-edge state, leading to $\gamma_{\text{eff}}^{\text{Bulk}} > \gamma_{\text{eff}}^{\text{L-edge}}$. Since the lower-edge states propagate to the right whereas the corresponding bulk states propagate to the left, this imbalance results in relative attenuation of the edge states toward the right and relative amplification of the bulk states toward the left. Under OBC, these states hybridize and localize at the left boundary, consistent with the winding number. Because the lower-edge states are strongly localized at the edge

and the number of bulk states in this group is smaller than that of the edge states, the state density on the edge is much larger. Consequently, the bulk density in Fig. 5(f) is barely visible.

We now turn to the NHSE observed in the upper-edge states, which is called nonlocal non-Hermitian antichiral skin effect. The green dots in Fig. 6(a) and 6(b) belong to the upper loop in Fig. 6(b). The corresponding eigenstate for dot 1 (upper-edge state) and dot 2 (bulk state) are shown in Fig. 6(d). Although no gain or loss is directly applied to the upper edge, the bulk states have finite weight on the lossy lower edge, giving $\gamma_{\text{eff}}^{\text{Bulk}} < 0$, while $\gamma_{\text{eff}}^{\text{U-edge}} \approx 0$. Thus, $\gamma_{\text{eff}}^{\text{Bulk}} < \gamma_{\text{eff}}^{\text{U-edge}}$. Unlike the lower-edge case, here the upper-edge states are relatively amplified toward the right, whereas the bulk states are relatively attenuated toward the left. Therefore, under OBC the NHSE occurs, and the upper-edge states hybridize with some bulk states that are localized on the right side, as shown in Fig. 5(g).

Note that in the limit $N_y \rightarrow \infty$, the loss at the lower edge has little effect on the bulk states, leading to $\gamma_{\text{eff}}^{\text{Bulk}} \rightarrow 0$. In this limit, the NHSE of the upper-edge states disappears, while that of the lower-edge states persists.

These are the physical mechanisms underlying the HSTE in the antichiral edge states. It is important to note that the mechanism of the HSTE is different between chiral and antichiral edge states. In previous studies [11, 12, 17, 18], the NHSE in chiral edge states originates from the hybridization of two adjacent chiral edge states and localizes at the so-called *domain wall of dissipation*, i.e., the spatial interface where the dissipation profile changes [17, 18]. However, because antichiral edge states do not exist simultaneously at both the left and right edges of the system, the lower and upper antichiral edge states can only couple to the counter-propagating bulk states. Consequently, the NHSE of antichiral edge states arises from the interplay between the antichiral edge states and the oppositely propagating bulk states, rather than from the antichiral edge states alone. Unlike systems with chiral edge states, the domain wall between the antichiral edge states and the bulk states is difficult to define, because the bulk states spread over the entire system.

Finally, we explain the NHSE occurring in the bulk states other than those enclosed by the blue dashed rectangle in Fig. 6(a), which are shown in Fig. 5(h). Under PBC, these states include bulk states propagating in both the left and right directions. However, for the states with the same $\text{Re}[E]$, the states propagating to the left [e.g., the top panels of Figs. 6(e) and 6(f)] have larger weight on the lower edge than those propagating to the right [e.g., the bottom panels of Figs. 6(e) and 6(f)]. As in the emergence of antichiral edge states, this effect is also induced by the presence of ϕ . In Fig. 6(a), the two Dirac points (corresponding to both endpoints of the edge states) are shifted in the vertical direction by ϕ [28]. As a result, for states with the same $\text{Re}[E]$, eigenstates

with $v_x > 0$ are located closer to the Dirac points. On the E_1 and E_2 bands, bulk states near the Dirac points tend to be more strongly distributed on edges. Therefore, eigenstates with $v_x > 0$ have larger weight on the edges. For eigenstates with the same $\text{Re}[E]$, defining the effective gain/loss of right- and left-propagating states as $\gamma_{\text{eff}}^{\text{right}}$ and $\gamma_{\text{eff}}^{\text{left}}$, respectively, we obtain $\gamma_{\text{eff}}^{\text{left}} > \gamma_{\text{eff}}^{\text{right}}$. Since a right-attenuating state and a left-amplifying state are coupled under OBC, the eigenstates become localized on the left side. This is the physical explanation of the NHSE induced solely by bulk states [Fig. 5(h)]. Note that, as in the case of the NHSE in the upper-edge states, the NHSE of the bulk states also disappears when the system size along the y direction is sufficiently large, because for large N_y the loss sites at the lower edge have little influence on the bulk states, leading to $\gamma_{\text{eff}}^{\text{left}} = \gamma_{\text{eff}}^{\text{right}}$ in the limit $N_y \rightarrow \infty$. It follows that the NHSE of the bulk states originates from the finite width of the system.

C. Upper-edge gain

In this subsection, we consider the Hamiltonian $H(\gamma_1 = 0, \gamma_2 = +0.6)$, shown in Fig. 7(a). According to Eq. (2), this system is the \mathcal{PT} counterpart of $H(\gamma_1 = -0.6, \gamma_2 = 0)$, namely,

$$(PT)H(\gamma_1 = 0, \gamma_2 = +0.6)(PT)^{-1} = H(\gamma_1 = -0.6, \gamma_2 = 0). \quad (13)$$

From Eq. (5), it follows that the eigenenergies of $H(\gamma_1 = 0, \gamma_2 = 0.6)$ are the complex conjugates of those of $H(\gamma_1 = -0.6, \gamma_2 = 0)$, and the corresponding eigenstates are related by the \mathcal{PT} operation.

Fig. 7(b) shows the band structure under PBC. As in the previous subsection, we focus on the two bands $E_1(k_x)$ and $E_2(k_x)$, whose complex-energy spectrum is shown in Fig. 7(c). This spectrum is the complex conjugate of Fig. 5(d); accordingly, all winding numbers change sign. The energy spectrum under OBC is shown in Fig. 7(d), which is likewise the complex conjugate of Fig. 5(e).

Figs. 7(e)–(g) display the spatial distributions of the lower-edge, upper-edge, and bulk states corresponding to the red points in Fig. 7(d), originating from E_1 and E_2 . In principle, these states are related to those in Fig. 5 by the \mathcal{PT} transformation. However, since the left and right boundaries are not strictly identical under OBC, the \mathcal{PT} symmetry is not exact in the finite system. Nevertheless, the direction of the NHSE is correctly reversed, consistent with the \mathcal{PT} mapping.

We now provide a physical interpretation of the NHSE in this case. The underlying mechanism is essentially the same as in the case of $H(\gamma_1 = -0.6, \gamma_2 = 0)$.

First, we consider the NHSE of the upper-edge states and the lower-edge states. Since gain is applied only to the upper edge, the effective gain/loss satisfies $\gamma_{\text{eff}}^{\text{U-edge}} > \gamma_{\text{eff}}^{\text{Bulk}} > \gamma_{\text{eff}}^{\text{L-edge}}$. This hierarchy is analogous to that in

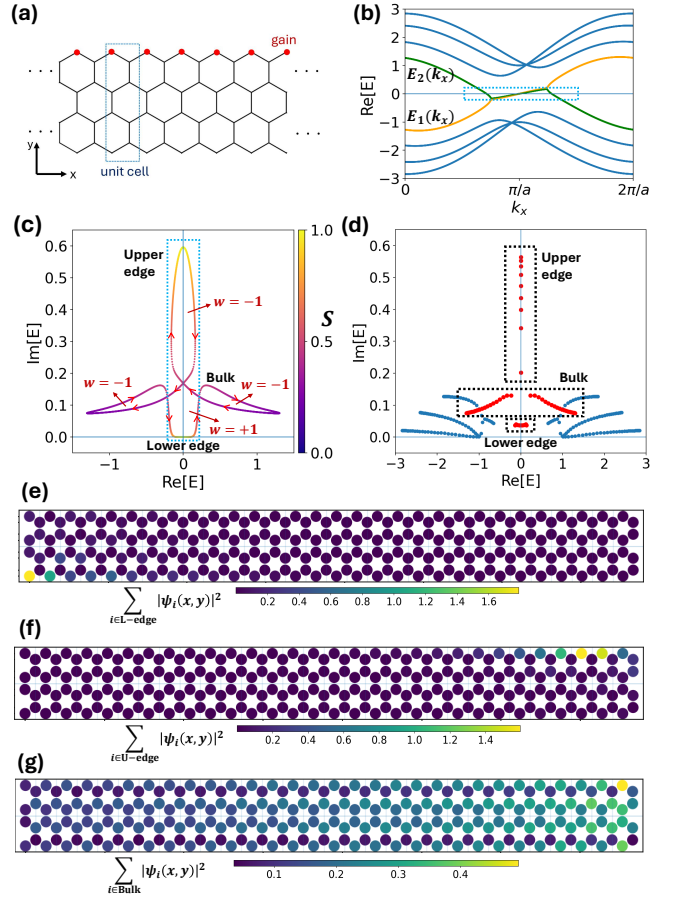


FIG. 7. Results for $H(\gamma_1 = 0, \gamma_2 = +0.6)$, the \mathcal{PT} -counterpart of Fig. 5. (a) Schematic of the system. (b) Band structure of $\text{Re}[E]$ under PBC along the x direction. (c) Complex-energy spectrum of E_1 and E_2 under PBC. The red arrows indicate the direction of each loop as k_x increases, and w denotes the point-gap winding number. (d) Energy spectrum under OBC along x . (e) Spatial distribution of the summed lower-edge states enclosed by the dashed rectangle in (d). (f) Spatial distribution of the summed upper-edge states enclosed by the dashed rectangle in (d). (g) Spatial distribution of the summed bulk states enclosed by the dashed rectangle in (d). Panels (c)–(g) correspond to Fig. 5(d)–5(h), but with opposite winding number and reversal localization directions due to the \mathcal{PT} transformation.

the previous subsection. Consequently, the localization directions of edge states are same to those in the lower-edge-loss case.

We next examine the NHSE of the bulk states. As shown in Fig. 8, eigenstates with $v_x > 0$ have larger weights near the edges than those with $v_x < 0$. Because the upper edge now carries gain, right-propagating states experience stronger amplification than left-propagating states, leading to $\gamma_{\text{eff}}^{\text{left}} < \gamma_{\text{eff}}^{\text{right}}$. Thus, the bulk states are localized on the right side of the system.

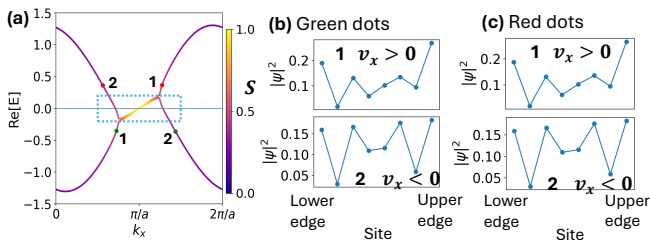


FIG. 8. Spatial profiles of representative eigenstates under PBC for $H(\gamma_1 = 0, \gamma_2 = +0.6)$. (a) Band structures of $\text{Re}[E_1]$ and $\text{Re}[E_2]$. (b) Spatial profiles of the two green dots in (a). (c) Spatial profiles of the two red dots in (a). In (b) and (c), the displayed region corresponds to the sites within the unit cell shown in Fig. 7(a). v_x denotes the group velocity along the x direction of the state shown.

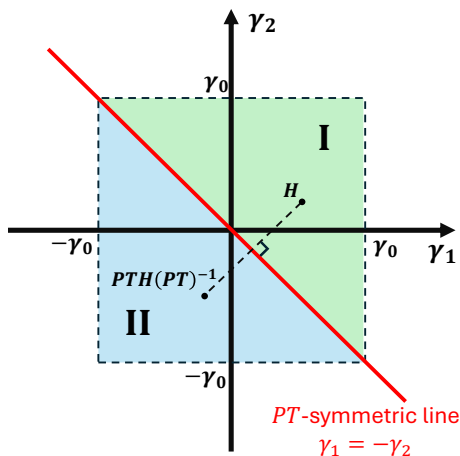


FIG. 9. Phase diagram of the NHSE in the (γ_1, γ_2) plane. The red line $\gamma_1 = -\gamma_2$ corresponds to the \mathcal{PT} -symmetric regime, where the bulk NHSE is forbidden. For $|\gamma_1| = |\gamma_2| < \gamma_0$, all bulk states remain in the \mathcal{PT} -symmetric phase. The \mathcal{PT} -symmetric line separates Phase I ($\gamma_1 + \gamma_2 > 0$) and Phase II ($\gamma_1 + \gamma_2 < 0$), in which the bulk skin modes localize at opposite boundaries. The two phases are related by the \mathcal{PT} transformation.

D. Phase diagram of the bulk NHSE

In Figs. 4, 5, and 7, we present the spatial profiles of antichiral edge states and bulk states under OBC and identify the presence or absence of the NHSE in each case. From these results, we observe that the upper-edge states are localized on the right boundary, while the lower-edge states are localized on the left boundary. In contrast, the bulk states originating from E_1 and E_2 remain extended in the \mathcal{PT} -symmetric case ($\gamma_1 = -0.6, \gamma_2 = 0.6$) [Fig. 4(g)], localize on the left side for ($\gamma_1 = -0.6, \gamma_2 = 0$) [Fig. 5(h)], and localize on the right side for ($\gamma_1 = 0, \gamma_2 = +0.6$) [Fig. 7(g)].

In this subsection, we summarize these results in the phase diagram shown in Fig. 9. From Eq. (2), the Hamiltonian $H(\gamma_1, \gamma_2)$ possesses \mathcal{PT} symmetry along the line

$\gamma_1 = -\gamma_2$. As discussed in Sec. III A, there exists a critical value $\gamma_0 \approx 0.89$. When $|\gamma_1| = |\gamma_2| < \gamma_0$, all bulk states remain in the \mathcal{PT} -symmetric phase, whereas the antichiral edge states belong to the \mathcal{PT} -broken phase. In what follows, we restrict our attention to the regime $|\gamma_{1,2}| < \gamma_0$.

The \mathcal{PT} -symmetric line $\gamma_1 + \gamma_2 = 0$ divides this region into two parts, denoted as Phase I and Phase II. According to Eq. (2), the Hamiltonians in these two phases are related by the \mathcal{PT} transformation.

In Phase I ($\gamma_1 + \gamma_2 > 0$), the two edges provide a net gain to the system. Since bulk states extend over both edges, their eigenenergies satisfy $\text{Im}[E] \geq 0$. Under OBC, the bulk states originating from E_1 and E_2 localize on the right boundary. This follows from the fact that right-propagating states have larger weight near the edges and therefore experience stronger amplification than left-propagating states, resulting in directional localization.

In Phase II ($\gamma_1 + \gamma_2 < 0$), the situation is reversed: the system has a net loss and the bulk eigenenergies satisfy $\text{Im}[E] \leq 0$. Under OBC, the bulk states originating from E_1 and E_2 localize on the left boundary.

The NHSE directions of the bulk states belonging to other bands are discussed in Appendix B.

Finally, we comment on the antichiral edge states. Unlike the bulk states, their localization direction cannot be determined solely from the phase diagram in Fig. 9. The localization of the upper (lower) edge states depends on the relative magnitude of the effective gain/loss of the edge states, $\gamma_{\text{eff}}^{\text{edge}}$, and that of the counter-propagating bulk states, $\gamma_{\text{eff}}^{\text{bulk}}$. Because $\gamma_{\text{eff}}^{\text{bulk}}$ depends on the detailed spatial distribution of the bulk states, the edge-state localization direction cannot be expressed in a simple global phase diagram.

IV. CONCLUSION

In this work, we have investigated a narrow non-Hermitian modified Haldane nanoribbon with gain and loss applied at the zigzag edges, and analyzed the non-Hermitian skin effect (NHSE) in both antichiral edge states and bulk states.

First, we clarified the mechanism underlying the hybrid skin-topological effect (HSTE) in the antichiral systems. In contrast to the conventional HSTE in chiral systems, where the NHSE originates from the interplay of edge modes at the dissipation domain walls, the HSTE in the present antichiral system arises from the competition between the antichiral edge states and the counter-propagating bulk states. The localization direction of the antichiral edge states is determined by the relative magnitude of the effective gain/loss experienced by the edge states and by the bulk states propagating in the opposite direction.

Second, we established the role of the \mathcal{PT} symmetry in organizing the bulk NHSE. In the \mathcal{PT} -symmetric

regime, the bulk eigenenergies remain real and no point gap opens, thereby forbidding the bulk NHSE. Once \mathcal{PT} symmetry is broken by tuning the edge gain and loss, the nonlocal non-Hermitian antichiral skin effect and the bulk NHSE emerge. The \mathcal{PT} -symmetric line separates two distinct bulk-skin phases characterized by opposite localization directions.

Our results demonstrate that edge-localized dissipation can serve as a symmetry-based control mechanism for non-Hermitian skin effects in the modified Haldane model. More broadly, this work highlights the quantitative differences between chiral and antichiral topological structures in non-Hermitian settings and provides a framework for engineering controllable skin modes via boundary design. Our model may be experimentally realizable in synthetic platforms such as photonic crystals or topoelectrical circuits, where gain and loss can be engineered in a controlled manner.

ACKNOWLEDGMENT

SU is supported by JST PRESTO (JPMJPR2351) and JSPS KAKENHI (JP25K07191).

Appendix A: \mathcal{PT} -symmetric system with large gain and loss

In this Appendix, we present the results for the Hamiltonian $H(\gamma_1 = -1, \gamma_2 = +1)$. In this case, $|\gamma_1| = |\gamma_2| > \gamma_0 \approx 0.89$, and some bulk states enter the \mathcal{PT} -broken phase.

Fig. 10(a) shows the complex-energy spectrum under PBC. The spatial distributions within a unit cell for the representative green and red points are shown in Fig. 10(c) and 10(d), respectively. These results indicate that bulk states in the \mathcal{PT} -broken phase become spatially biased toward either the upper or lower side of the ribbon. Such states form loops together with certain bulk states that remain in the \mathcal{PT} -symmetric phase.

Under OBC, these loops collapse into line segments, as shown in Fig. 10(b). The summed spatial distributions of the green (red) dots are shown in Fig. 10(e) [Fig. 10(f)]. The green (red) states localize on the right (left) boundary, exhibiting a bipolar skin effect [45–47], where distinct groups of states accumulate at opposite boundaries.

The physical origin of the NHSE can be understood as follows. Consider, for example, the green states in Fig. 10(a). Under OBC, these states arise from the hybridization between a \mathcal{PT} -broken-phase state that is predominantly localized near the upper side and propagates to the right, and a \mathcal{PT} -symmetric bulk state that is distributed more uniformly and propagates to the left. Since the upper side carries gain while the lower side carries loss, the effective gain/loss satisfies $\gamma_{\text{eff}}^{\text{right}} > \gamma_{\text{eff}}^{\text{left}} = 0$. As a result, the right-propagating component is amplified. Therefore, these states are localized on the right

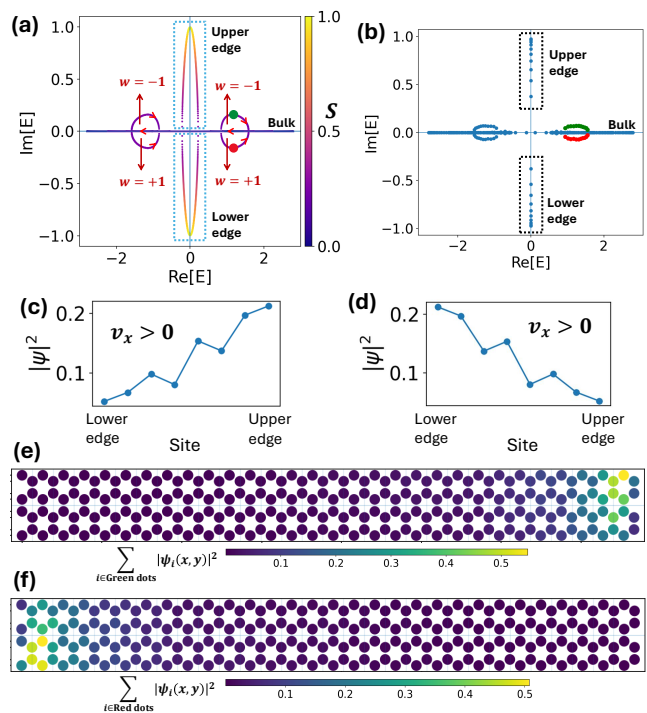


FIG. 10. Results for $H(\gamma_1 = -1, \gamma_2 = +1)$, where $|\gamma_1| = |\gamma_2| > \gamma_0$. (a) Complex-energy spectrum under PBC along the x direction. The red arrows indicate the direction of each loop as k_x increases, and w denotes the point-gap winding number. Brighter colors indicate stronger localization at the upper and lower edges. The system size is $N_x = 1600$. (b) Energy spectrum under OBC along x . (c) Spatial profiles of the green dot in (a). (d) Spatial profiles of the red dot in (a). In (c) and (d), v_x denotes the group velocity along the x direction of the state shown. (e) Spatial distribution of the summed bulk states corresponding to the green points in (b). (f) Spatial distribution of the summed bulk states corresponding to the red points in (b). In (e) and (f), brighter colors indicate higher state density. The system size is $N_x = 30$.

side. This interpretation is consistent with the winding numbers shown in Fig. 10(a).

These results demonstrate that when $|\gamma_1| = |\gamma_2| > \gamma_0$, some bulk states enter the \mathcal{PT} -broken phase and the NHSE emerges even along the \mathcal{PT} -symmetric line.

Appendix B: Bulk NHSE in bands other than E_1 and E_2

In this Appendix, we present bulk eigenstates of $H(\gamma_1 = -0.6, \gamma_2 = 0)$ under OBC that belong to bands other than E_1 and E_2 shown in Fig. 5(b). These bulk states also exhibit the NHSE due to the finite ribbon width and the presence of edge loss.

We label the relevant bands as E_3 – E_8 as shown in Fig. 11(a). The corresponding complex-energy spectrum under PBC is shown in Fig. 11(b). Bands E_4 , E_5 , E_6 , and E_7 form point gaps with $w = -1$, implying localiza-

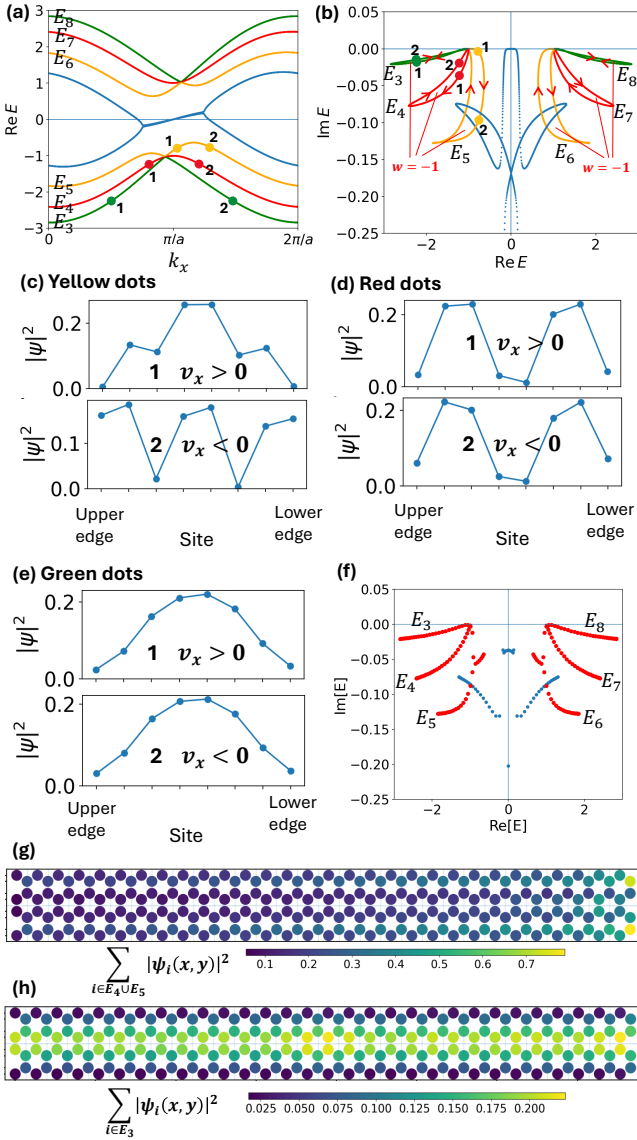


FIG. 11. Bulk NHSE in bands other than E_1 and E_2 for $H(\gamma_1 = -0.6, \gamma_2 = 0)$. (a) Band structure of $\text{Re}[E]$ under PBC along the x direction, highlighting the bands $E_3 - E_8$. (b) Complex-energy spectrum under PBC. The red arrows indicate the direction of each loop as k_x increases, and w denotes the point-gap winding number. The system size is $N_x = 1600$. (c) Spatial profiles of the two yellow dots in (a) and (b). (d) Spatial profiles of the two red dots in (a) and (b). (e) Spatial profiles of the two green dots in (a) and (b). In (c)-(e), v_x denotes the group velocity along the x direction of the state shown. (f) Energy spectrum under OBC along x . Red dots indicate eigenenergies originating from $E_3 - E_8$. (g) Spatial distribution of the summed bulk states originating from E_4 and E_5 . (h) Spatial distribution of the summed bulk states originating from E_3 . In (g) and (h), brighter colors indicate higher state density. The system size is $N_x = 30$.

tion on the right boundary under OBC. As an example, Fig. 11(g) shows the summed spatial distribution of the OBC states originating from E_4 and E_5 , confirming their localization on the right side.

On the other hand, as seen in Fig. 11(b), E_3 and E_8 exhibit only very small point gaps. In fact, Fig. 11(h), which shows the summed OBC states of E_3 , indicates that these states remain nearly extended. Although a weak NHSE is expected in principle, it is practically negligible.

The physical origin of this behavior can be understood from the spatial structure of the eigenstates. As shown in Figs. 11(c) and 11(d), for states with the same $\text{Re}[E]$ in E_4 and E_5 , those with $v_x < 0$ have larger weight near the lower edge than those with $v_x > 0$. Since the lower edge carries loss, this leads to $\gamma_{\text{eff}}^{\text{left}} < \gamma_{\text{eff}}^{\text{right}}$. Under OBC, this imbalance causes localization on the right boundary.

By contrast, as shown in Fig. 11(e), the states in E_3 are distributed predominantly around the center of the ribbon and have negligible weight on the edges. Consequently, the edge loss has little influence on these states, and the NHSE is suppressed.

Combining these results with those in Sec. III B, we conclude that the bulk states originating from E_1 and E_2 localize on the left boundary, whereas the other bulk states either localize on the right boundary or remain nearly extended. This coexistence of oppositely localized bulk modes constitutes a bipolar skin effect.

$H(\gamma_1 = -0.6, \gamma_2 = 0)$ belongs to phase II, which is defined in Sec. III D. In phase I, the localization direction of each band is reversed under the \mathcal{PT} transformation.

[1] K. Kawabata, K. Shiozaki, M. Ueda, and M. Sato, Symmetry and topology in non-hermitian physics, Phys. Rev.

- [2] Y. Ashida, Z. Gong, and M. Ueda, Non-hermitian physics, *Adv. Phys.* **69**, 249 (2020).
- [3] H. Shen, B. Zhen, and L. Fu, Topological band theory for non-hermitian hamiltonians, *Phys. Rev. Lett.* **120**, 146402 (2018).
- [4] N. Okuma, K. Kawabata, K. Shiozaki, and M. Sato, Topological origin of non-hermitian skin effects, *Phys. Rev. Lett.* **124**, 086801 (2020).
- [5] K. Zhang, Z. Yang, and C. Fang, Correspondence between winding numbers and skin modes in non-hermitian systems, *Phys. Rev. Lett.* **125**, 126402 (2020).
- [6] W. Zhu and L. Li, A brief review of hybrid skin-topological effect, *J. Phys.: Condens. Matter* **36**, 253003 (2024).
- [7] R. Lin, T. Tai, L. Li, and C. H. Lee, Topological non-hermitian skin effect, *Front. Phys.* **18**, 53605 (2023).
- [8] C. H. Lee, L. Li, and J. Gong, Hybrid higher-order skin-topological modes in nonreciprocal systems, *Phys. Rev. Lett.* **123**, 016805 (2019).
- [9] Z. Ou, Y. Wang, and L. Li, Non-hermitian boundary spectral winding, *Phys. Rev. B* **107**, L161404 (2023).
- [10] H. Wakao, Hybrid higher-order skin topological modes in the two-dimensional su–schrieffer–heeger model with nonreciprocal hoppings, *J. Phys. Soc. Jpn.* **93**, 064702 (2024).
- [11] W. Zhu and J. Gong, Hybrid skin-topological modes without asymmetric couplings, *Phys. Rev. B* **106**, 035425 (2022).
- [12] Y. Li, C. Liang, C. Wang, C. Lu, and Y.-C. Liu, Gain-loss-induced hybrid skin-topological effect, *Phys. Rev. Lett.* **128**, 223903 (2022).
- [13] Y.-L. Zhang, L.-W. Wang, Y. Liu, Z.-X. Chen, and J.-H. Jiang, Hybrid skin-topological effect in non-hermitian checkerboard lattices with large chern numbers (2024), arXiv:2411.07465 [physics.optics].
- [14] J. Sun, C.-A. Li, S. Feng, and H. Guo, Hybrid higher-order skin-topological effect in hyperbolic lattices, *Phys. Rev. B* **108**, 075122 (2023).
- [15] S. Li, L. Dou, C. Zhang, T. Jiang, Z. Wei, Z. Wang, and X. Cheng, Hybrid skin-topological-anderson effect in systems with gain and loss, *Commun. Phys.* **8**, 431 (2025).
- [16] R. Bao, R. Banerjee, S. Mandal, H. Xu, S. Li, J. Gao, and T. C. H. Liew, Exciton-polariton hybrid skin-topological states (2025), arXiv:2512.01768 [cond-mat.mes-hall].
- [17] T.-R. Liu, T. Liu, and M. Xiao, Anomalous non-hermitian skin effect of chiral boundary states, *Phys. Rev. B* **112**, L081112 (2025).
- [18] X.-R. Ma, K. Cao, X.-R. Wang, Z. Wei, Q. Du, and S.-P. Kou, Non-hermitian chiral skin effect, *Phys. Rev. Research* **6**, 013213 (2024).
- [19] F. Schindler, K. Gu, B. Lian, and K. Kawabata, Hermitian bulk–non-hermitian boundary correspondence, *PRX Quantum* **4**, 030315 (2023).
- [20] D. Nakamura, K. Inaka, N. Okuma, and M. Sato, Universal platform of point-gap topological phases from topological materials, *Phys. Rev. Lett.* **131**, 256602 (2023).
- [21] G.-G. Liu *et al.*, Localization of chiral edge states by the non-hermitian skin effect, *Phys. Rev. Lett.* **132**, 113802 (2024).
- [22] Y. Sun *et al.*, Photonic floquet skin-topological effect, *Phys. Rev. Lett.* **132**, 063804 (2024).
- [23] D. Zou *et al.*, Observation of hybrid higher-order skin-topological effect in non-hermitian topoelectrical circuits, *Nat. Commun.* **12**, 7201 (2021).
- [24] T. Jiang, C. Zhang, R.-Y. Zhang, Y. Yu, Z. Guan, Z. Wei, Z. Wang, X. Cheng, and C.-T. Chan, Observation of non-hermitian boundary induced hybrid skin-topological effect excited by synthetic complex frequencies, *Nat. Commun.* **15**, 10863 (2024).
- [25] J. Wu *et al.*, Spin-dependent localization of helical edge states in a non-hermitian phononic crystal, *Phys. Rev. Lett.* **133**, 126601 (2024).
- [26] Y.-X. Fang, W.-H. Zhu, Y.-P. Lai, Y. Li, and S.-Q. Wu, Tunable hinge skin states in a hybrid skin-topological sonic crystal, *Phys. Rev. B* **113**, 035407 (2026).
- [27] L. S. Palacios *et al.*, Guided accumulation of active particles by topological design of a second-order skin effect, *Nat. Commun.* **12**, 4691 (2021).
- [28] E. Colomés and M. Franz, Antichiral edge states in a modified haldane nanoribbon, *Phys. Rev. Lett.* **120**, 086603 (2018).
- [29] F. D. M. Haldane, Model for a quantum hall effect without landau levels: Condensed-matter realization of the “parity anomaly”, *Phys. Rev. Lett.* **61**, 2015 (1988).
- [30] R. Ye, Y. He, G. Li, L. Wang, X. Wu, X. Qiao, Y. Zheng, L. Jin, D.-W. Wang, L. Yuan, and X. Chen, Observation of non-hermitian antichiral edge currents, *Light Sci. Appl.* **14**, 39 (2025).
- [31] R.-J. Chen, G.-Q. Zhang, Z. Li, and D.-W. Zhang, Antichiral and trap-skin dynamics in a nonreciprocal bosonic two-leg ladder with artificial magnetic flux, *Phys. Rev. A* **110**, 043311 (2024).
- [32] M. Mannai and S. Haddad, Strain tuned topology in the haldane and the modified haldane models, *J. Phys.: Condens. Matter* **32**, 225501 (2020).
- [33] M. M. Denner, J. L. Lado, and O. Zilberberg, Antichiral states in twisted graphene multilayers, *Phys. Rev. Res.* **2**, 043190 (2020).
- [34] T. Mizoguchi and T. Koma, Bulk-edge correspondence in two-dimensional topological semimetals: A transfer matrix study of antichiral edge modes, *Phys. Rev. B* **103**, 195310 (2021).
- [35] X. Cheng, J. Chen, L. Zhang, L. Xiao, and S. Jia, Antichiral edge states and hinge states based on the haldane model, *Phys. Rev. B* **104**, L081401 (2021).
- [36] R. Bao, S. Mandal, H. Xu, X. Xu, R. Banerjee, and T. C. H. Liew, Spin-polarized antichiral exciton-polariton edge states, *Phys. Rev. B* **106**, 235310 (2022).
- [37] S. Cheng, Fragility of antichiral edge states in a modified haldane model, *Phys. Rev. B* (2026).
- [38] L. Xie, T. He, and L. Jin, Synchronized in-gap edge states and robust copropagation in topological insulators without magnetic flux, *Fundamental Research* (2025), in Press, corrected proof (available online 21 Jan 2025); arXiv:2504.17231.
- [39] G. F. R. Ruiz, J. H. Mateos, L. Tosi, C. Strunk, C. Balsero, and L. Arrachea, Antichiral edge states and bogoliubov fermi surfaces in a two-dimensional proximity-induced superconductor, *Phys. Rev. B* **112**, L241409 (2025).
- [40] X.-H. Wei, X.-W. Luo, M. Yang, Y.-W. Liao, J.-S. Xu, G.-C. Guo, and Z.-W. Zhou, Tunable antichiral hinge state in photonic synthetic dimensions (2025), arXiv:2506.17643 [quant-ph].
- [41] P. Zhou, G.-G. Liu, Y. Yang, Y.-H. Hu, S. Ma, H. Xue, Q. Wang, L. Deng, and B. Zhang, Observation of photonic antichiral edge states, *Phys. Rev. Lett.* **125**, 263603 (2021).

- (2020).
- [42] Y. T. Yang, D. J. Zhu, Z. H. Hang, and Y. D. Chong, Observation of antichiral edge states in a circuit lattice, *Sci. China Phys. Mech. Astron.* **64**, 257011 (2021).
- [43] Z. Lei, C. H. Lee, and L. Li, Activating non-hermitian skin modes by parity-time symmetry breaking, *Commun. Phys.* **7**, 100 (2024).
- [44] To clarify the correspondence between the spectra under PBC and OBC, we continuously deform the boundary condition by multiplying the hopping terms connecting the left and right boundaries by a parameter λ , varying it from $\lambda = 1$ (PBC) to $\lambda = 0$ (OBC).
- [45] Q.-B. Zeng, Non-hermitian skin effect edge, *Phys. Rev. B* **106**, 235411 (2022).
- [46] W.-C. Jiang, J. Li, Q.-X. Li, and J.-J. Zhu, The reciprocating and bipolar non-hermitian skin effect engineered by spin-orbit coupling, *Appl. Phys. Lett.* **123**, 201107 (2023).
- [47] W.-C. Jiang, H. Wu, Q.-X. Li, J. Li, and J.-J. Zhu, Tunable non-hermitian skin effect via gain and loss, *Phys. Rev. B* **110**, 155144 (2024).
- [48] M. Vila, N. T. Hung, S. Roche, and R. Saito, Tunable circular dichroism and valley polarization in the modified haldane model, *Phys. Rev. B* **99**, 161404 (2019).